SHORT COMMUNICATION

Optofluidic device for ultra-sensitive detection of proteins using surface-enhanced Raman spectroscopy

Miao Wang · Melodie Benford · Nan Jing · Gerard Coté · Jun Kameoka

Abstract An optofluidic device is reported in this paper that can highly improve the robustness of surface-enhanced Raman scattering (SERS) detection and provide fingerprint information of proteins with a concentration in the nanogram per liter range within minutes. Moreover, the conformational change of protein can also be obtained using this device. Fabricated by standard photolithography processes, the optofluidic device has a step microfluidic–nanofluidic structure, which provides robust SERS detection. The sensitivity of the device is investigated using insulin and albumin as target analytes at a concentration of 0.9 ng/L. The ability to detect conformational changes of proteins using this technology is also shown by probing these analytes before and after their denaturation.

Keywords Optofluidic · Nanofluidic · Protein · Conformational change · SERS

Abbreviations

SERS	Surface-enhanced Raman scattering
A-Si	Amorphous silicon
PECVD	Plasma-enhanced chemical vapor deposition
HF	Hydrofluoric
CF_4	Tetrafluoride
BSA	Bovine serum albumin
RT	Room temperature

M. Wang · N. Jing · J. Kameoka (✉)
Department of Electrical Engineering, Texas A&M University,
College Station, TX 77843-3128, USA
e-mail: kameoka@ece.tamu.edu

M. Benford · G. Coté
Department of Biomedical Engineering, Texas A&M University,
College Station, TX 77843-3120, USA

1 Introduction

Traditionally, dispersive Raman spectroscopy has been used for chemical detection. However in its native form, it is an inefficient tool for the detection of bioanalytes. This is due to the relatively low number of Raman scattered photons compared to Rayleigh scattered ones (Stevenson and Vo-Dinh 1996). Broadband fluorescence signals of higher intensity (several orders of magnitude) from the molecule of interest as well as other surrounding molecules can drown out the Raman signals (Kneipp et al. 2002). All of these factors demand the presence of highly sophisticated and powerful lasers, spectrometers, array and imaging detectors and digital electronics in order to use Raman spectroscopy for analyte detection at trace levels. In contrast, surface-enhanced Raman scattering (SERS) is a well-known technique in which the spectroscopic signature of molecules obtained through Raman scattering can be greatly enhanced or modified in the vicinity of metal surfaces or structures.

SERS was reported in the 1970s as a phenomenon in which light was directed at analytes on roughened metal electrodes (Fleischman et al. 1974; Pemberton and Buck 1981; Pettinger et al. 1980). The SERS technique was later expanded to include metal nanoparticles/colloids (Abe et al. 1981; Kneipp et al. 1997; Nie and Emory 1997), metal nanoparticle arrays (Félidj et al. 2003, 2004; Gunnarsson et al. 2001; Wang et al. 2005), metal nanorods (Chaney et al. 2005; Nikoobakht and El-Sayed 2003) and metal-coated structures (Dick et al. 2002; Kubo et al. 2002; Oldenburg et al. 1999). Although the enhancement mechanism is not fully understood, two effects are generally credited in literature to contribute to the enhancement, namely the electromagnetic effect and the chemical effect (Gersten and Nitzan 1980; Hering et al. 2008; Kneipp et al.

1999). Electromagnetic resonances in metal nanostructures, currently named localized surface plasmons, has been generally accepted as a basic SERS mechanism, since it can be used to explain many SERS phenomena. These include the need for nanoscale features within SERS substrates, the effect of different metal and excitation frequency on the enhancement, and the dependence of enhancement on the size, shape and interspacing of nanostructures (Campion and Kambhampati 1998; Emory et al. 1998; Gunnarsson et al. 2001; Moskovits 2005; Zeman and Schatz 1987). SERS intensity can be greatly increased when two or more nanoparticles are brought in close proximity to each other because of the electromagnetic coupling effect (Gunnarsson et al. 2001; Su et al. 2003). The chemical mechanism involves a charge transfer process between the analytes and metal nanostructure (Moskovits 2005; Otto 2005). The overall enhancement factor ranges from 10^4 to 10^{15} (Hering et al. 2008).

Especially high enhancement factors have been reported for single molecule detection using SERS at so-called "hot spot" sites (Kneipp et al. 1997, 1998; Nie and Emory 1997). However, the distribution of hot spots is not uniform and therefore it is difficult to predict where the hot spots will occur and the level of SERS enhancement. In our research, we have developed an optofluidic device that can overcome this problem by physically trapping metal

nanoparticles and analytes at a specific location (Chou et al. 2008; Wang et al. 2007). The close-packed nanoparticles can generate condensed hot spots, which can provide a large enhancement factor. The location of the hot spot can be controlled and predicted rather than randomly distributed. Thus, reproducible and consistent SERS signals can be collected. This device has also achieved ultrasensitive detection of analytes with a concentration in the pico-molar range and the required volume of the sample solutions has been decreased to microliters. In this paper, we present the fabrication and use of this device to detect low concentrations and describe conformational changes of target proteins due to denaturation.

2 Experimental

2.1 Fabrication of the optofluidic device

The optofluidic device has a pinched micro–nano fluidic structure, which enables trapping of the nanoparticles. A photolithography process was used to fabricate the optofluidic device. The substrate was a double-side polished fused silica wafer with a thickness of 500 μm (Mark Optics Inc., Santa Ana, CA). The fabrication process is shown in Fig. 1. Initially, the first layer of photoresist was

Fig. 1 Schematic diagram of fabrication process for the optofluidic device

Side View	Top View	Fabrication Flow
fused silica wafer	Fused silica	4" fused silica wafer
photoresist (PR1) / fused silica wafer	PR1	Spin coat photoresist (PR1)
PR1 / fused silica wafer	—	UV exposure and develop
PR1 / fused silica wafer	—	Dry etch to 40nm
photoresist(PR2) / A-Si layer	PR2	Strip of PR1, PECVD deposited A-Si layer and spin coat a 2nd layer PR2
PR2 / A-Si layer / fused silica wafer		Align, pattern and develop
PR2 / A-Si layer / fused silica wafer		Remove A-Si layer by CF₄ reactive ion etching
PR2 / A-Si layer / fused silica wafer		Wet etch to 3μm
fused silica wafer		Remove PR & A-Si layer
fused silica wafer		Sand blasting inlet and outlet holes
fused silica wafer		Bond with another wafer

spin-coated on the substrate and a 2 μm width trench was patterned. It was then etched down to a 40 nm depth with dry etching. The photoresist was then stripped off and a layer of amorphous silicon (A-Si) was deposited onto the wafer using plasma-enhanced chemical vapor deposition (PECVD) to serve as a hard mask. A second layer of photoresist was spin-coated on the top of an A-Si layer. The microfluidic channel mask was then aligned with the nanofluidic channel, patterned and developed. The A-Si layer was selectively removed by carbon tetrafluoride (CF_4) reactive ion etching and concentrated hydrofluoric (HF) acid (49%) was used to create a 3 μm depth microfluidic trench. After removing the remaining A-Si layer and photoresist, the inlet and outlet holes were sandblasted through with fine alumina powders. Finally, the wafer was thoroughly cleaned and clung with an intact fused silica wafer using de-ionized water and annealed at 1,050°C for 6 h for permanent bonding. Plastic reservoirs were then attached around the inlet and outlet respectively using 5-min epoxy.

2.2 Working mechanism

A schematic diagram of the optofluidic device is shown in Fig. 2 The microfluidic channel has a depth of 3 μm and a width of 50 μm. The nanofluidic channel has a depth of 40 nm and a width of 2 μm.

In our experiment, gold nanoparticles with a diameter of 60 nm suspended in water were used as the SERS-active metal nanostructures. The gold nanoparticles were mixed with analyte solution and then dispensed into the inlet reservoir. The sample solution was drawn into the optofluidic device by capillary force. Since the size of gold nanoparticles is larger than the depth of nanofluidic channel, the

gold nanoparticles were trapped and formed into clusters at the entrance to the nanochannel. Furthermore, capillary force continued to bring analytes through the interstices of the gold clusters and created an area with locally high concentration of analytes around the gold clusters. The highly condensed gold clusters and high concentration of analytes contributed to especially high detection sensitivity.

While the depth of the nanochannel assures the reliable trapping of nanoparticles, the width of the nanofluidic channel was designed to be 3 μm to guarantee fast transportation of aqueous solution. The trapping process occurred within minutes after the sample solution was put into the inlet reservoir. Figure 3 shows the optical images of aggregation of gold nanoparticles over time. As the nanoparticles were trapped at the junction of microfluidic channel and nanofluidic channel, they formed into clusters as depicted by the black spot shown in the figure.

3 Results and discussion

Previously, we reported that this optofluidic device could provide an enhancement factor of 10^8 compared with an enhancement factor of 10^6 using a conventional SERS detection technique (Wang et al. 2007). Moreover, the concentration of gold nanoparticles and analytes at the aggregation site increases with time due to continuous capillary force, which further enhanced SERS intensity. An additional 10^5-fold increase due to nanoparticle/molecule concentration was reported (Wang et al. 2007). The performance of the optofluidic device has been confirmed with various samples (Chou et al. 2008; Wang et al. 2007). For example, it has been shown that adenine solution was detectable in the pico-molar range without any difficulty

Fig. 2 Schematic diagram of the optofluidic device showing the (**a**) side view and (**b**) top view
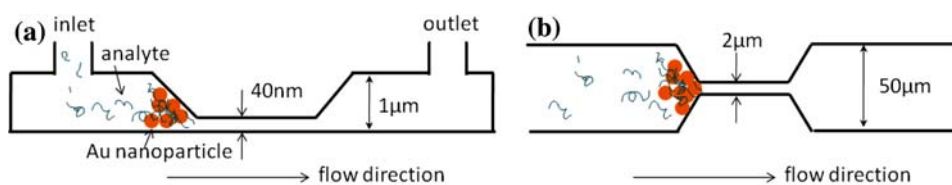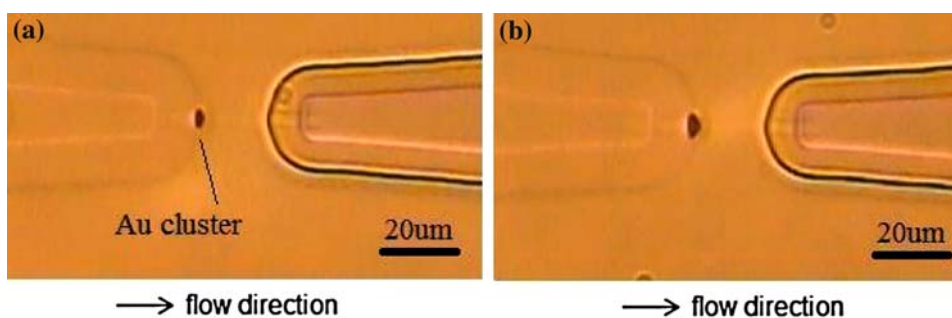
Fig. 3 Optical microscopic images showing aggregation of Au nanoparticles in an optofluidic device, **a** 3 min after adding sample and **b** 12 min after adding sample

(Wang et al. 2007). The device was also shown to be able to detect β-amyloid, which is a biomarker for Alzheimer's disease, at low concentration and, for the first time, to detect a conformational change in this analyte with this approach (Chou et al. 2008).

To explore the further applications of this optofluidic device, we used it to probe the spectra of two proteins, insulin from bovine pancreas and bovine serum albumin (BSA), at room temperature (RT) and elevated temperatures, to investigate the ability to detect denaturation of protein due to the heat. During heat denaturation, the secondary structure of proteins changes and the proteins unfold from their original form. Insulin and BSA were both purchased from Sigma-Aldrich. Insulin was in solution with a concentration of 10 mg/mL in 25 mM HEPES (pH 8.2) and BSA was in powder form. Before the experiment, the proteins were stored at 6°C. Before use, the proteins were diluted with DI water to 10 ng/L and a heated water bath was used to denature the proteins. Three samples of each protein were prepared: (1) at room temperature, (2) heated to 60°C and (3) heated to 100°C for 10 min. The samples were mixed with 60 nm gold nanoparticles (Polysciences, Inc.) and suspended in water at 1:10 volume ratio of protein solution to gold nanoparticles. This mixing diluted the sample concentration further to 0.9 ng/L for both proteins. Immediately after mixing, six samples (BSA at RT, BSA heated to 60°C, BSA heated to 100°C, insulin at RT, insulin at 60°C, and insulin at 100°C) with a volume of 5 μL each were dispensed into the inlet reservoirs of six independent optofluidic channels. Within 3 min, the aggregation of gold nanoparticles became visible under the microscope and SERS spectra were collected. The SERS data were collected using a HORIBA Jobin Yvon LabRam IR/Raman system with a 785 nm laser excitation. A 50× objective (NA = 0.45) lens was used to focus the light onto the gold clusters. The laser power on the sample was 70 μW. The scanning range was from 600 $\sim$ 1,600 cm^{-1} with an integration time of 60 s. Five spectra were collected from three samples for each protein, then normalized and averaged to get the final spectra profile. The spectra shown in Figs. 4 and 5 under different conditions were offset for visual clarity. The peaks, assigned as determined from the literature, are shown in Tables 1 and 2 (Miura and Thomas 1995; Miura et al. 2000; Podstawka et al. 2004; Stewart and Fredericks 1999; Tu 1982; Yu et al. 1972). The characteristic peaks for insulin and BSA at an ultra-low concentration are clearly identified by using the optofluidic channel and SERS detection. More importantly, the information due to the change of structure at different temperatures is also provided.

BSA is a globular protein, composed primarily of α-helices and random coils at room temperature (Shanmugam and Polavarapu 2004; Wetzel et al. 1980). With our optofluidic device, detection of BSA at 0.9 ng/L
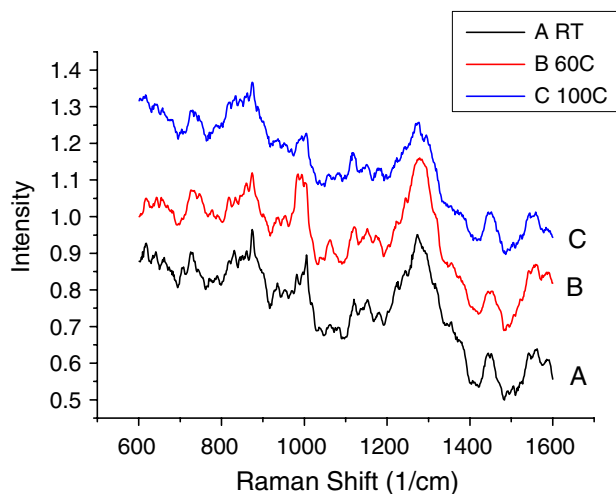
Fig. 4 SERS spectra of BSA at different temperatures (RT, 60, 100°C)
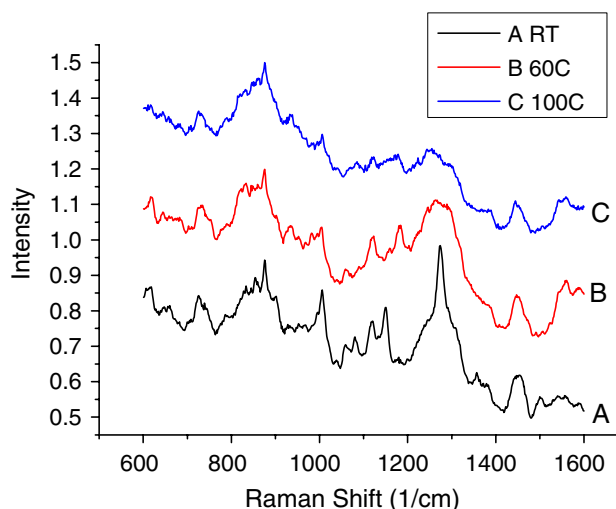
Fig. 5 SERS spectra of insulin at different temperatures (RT, 60, 100°C)

was achieved successfully. The averaged normalized spectra for different temperatures are shown in Fig. 4. The assignment of peaks for spectrum A, which is the BSA without heat, can be found in Table 1.

β-Sheet formation is expected at higher temperatures (>60°C) (Shanmugam and Polavarapu 2004), as is a concentration dependence of β-sheet formation with temperature (Shanmugam and Polavarapu 2004; Wetzel et al. 1980). From these three spectra, we can tell that as the temperatures increases, the structure of BSA is denatured and β-sheet structure is formed. There is an intense band at 1,277 cm^{-1}, indicating strong α-helical secondary structure. The intensity of this band decreases appreciably for samples heated at elevated temperatures, which indicates a loss in secondary structure and supports unfolding of the protein. The band, although diminished, still exists, suggesting that

Table 1 Assignment of peaks in BSA spectrum (RT)

Wavenumber	Assignment	
620	COO⁻ wag or phenylalanine	
643	Ring deformation	Tyr
662	C–S stretching vibration	Cys
730	COO⁻ def	Backbone
832	Stretching and ring breathing mode	Tyr
876	Indole ring	Trp
938	α-Helical C–C stretch	
957	C–C stretch	
993	Indole asymmetric breath	Trp
1007	Strong, "breathing" vibration of the benzene ring	Phe
1184		Phe, Tyr
1233	β-Sheet (amide III region)	
1254	Random coil (amide III region)	
1277	α-Helix (amide III region)	
1356	Indole vibration	Trp
1453	CH$_2$ bending/scissoring mode	
1564	Amide II band	
1593	COO⁻ asymmetric stretch	Backbone

Table 2 Assignment of peaks in insulin spectrum (RT)

Wavenumber	Assignment	
620	COO⁻ wag or phenylalanine	
662	C–S stretching vibration	Cys
835	Stretching and ring breathing mode,	Tyr doublet
855	Stretching and ring breathing mode	Tyr doublet
938	α-Helical C–C stretching vibration	
963	C-COO⁻ stretch	
1007	Stretching and benzyl ring breathing mode	Phe
1050	β-Sheet (amide III region)	
1066	C–N stretch	
1081	C–N stretch	
1121	NH$_3$+ deformation	
1151	NH$_3$+ deformation	
1276	α-Helix (amide III region)	
1311	CH$_2$ wag	
1457	CH$_2$ scissoring or bending mode	
1552	Amide II band	
1564	Amide II band	
1594	COO⁻ asymmetric stretch	Backbone

the ordered structure is not completely destroyed. For the sample heated to 60°C, this band, although still intense, broadens and shifts to the right. For the 100°C sample, a small shoulder develops at 1,296 cm⁻¹, indicative of β-

sheet structure (Tu 1982), which supports the hypothesis that some β-sheet structure may be formed upon thermal denaturation (Shanmugam and Polavarapu 2004; Wetzel et al. 1980). In addition, the medium band at 938 cm⁻¹ is tentatively assigned to skeletal C–C stretching vibration characteristic of α-helical conformation. This band decreases by about 25% in the 60°C spectra, and then by 50% in the 100°C, indicating an incomplete loss in α-helical content (Tu 1982). Furthermore, the amide III band, indicative of high α-helical content, still exists at the elevated temperature, although with a decreased intensity. Thus, it appears that heating the samples to 60 and 100°C does not completely denature the secondary structure of protein. Further, the 1,007 cm⁻¹ line, tentatively assigned to the breathing vibration of the benzene ring of phenylalanine, also decreases with temperature. This may be due to unfolding of the protein in which the phenylalanine residue is not close to the gold nanoparticle or adopts a parallel orientation relative to the surface, further supported by the low intensity of this stretching vibration (Podstawka et al. 2004). Medium bands at 730 cm⁻¹ attributed to carboxylate groups, broadened and shifted to 735 and 737 cm⁻¹, respectively, in the 60 and 100°C spectra, indicating more structural change. In addition, the band at 1,453 cm⁻¹ remains relatively the same, indicating that this methylene bending vibration is not sensitive to structure change (Tu 1982). On the other hand, the 662 cm⁻¹ band shifts to 659 cm⁻¹ for the sample heated to 60°C and then to 657 cm⁻¹ for 100°C. This is likely due to the rearrangement of the conformation of the disulfide bonds in BSA.

Insulin is also a globular protein, composed of two polypeptides (the α- and β-chain) joined by disulfide bonds, both exhibiting α-helical and random coil conformation (Jiang and Chang 2005). The spectra taken at different temperatures for insulin are shown in Fig. 5. The assignment of peaks for spectrum A, which is insulin before being heated, can be found in Table 2. Similar to BSA, its secondary structure was changed, but not completely destroyed by the heat. The sharp peak at 1,276 cm⁻¹ lies in the amide III region, which represents the N–H in-plane bending mode of the peptide bond (Lippert et al. 1976; Podstawka et al. 2004; Yu et al. 1972). Upon denaturation, the band decreases considerably and broadens into a shoulder. It is proposed that the insulin conformation exhibits some β-sheet conformation upon thermal denaturation (Yu et al. 1972), which is supported by the broadening of the band to include the 1,245 cm⁻¹ region at 100°C. This band is tentatively assigned to β-sheet and/or random coil conformation (Lippert et al. 1976; Podstawka et al. 2004; Yu et al. 1972).

The 640–680 cm⁻¹ region is a mixed vibration area, the small shifts, appearance, and disappearance of bands could also be attributed to conformational changes in the

disulfide bonds of the cysteine residues as also seen in the BSA spectra. The drastic change in the 1,050–1,200 cm^{-1} regions indicate an extreme unfolding of the protein backbone. The two small resolved peaks at 1,066 and 1,081 cm^{-1} (tentatively assigned to the stretching vibration of C–N) also disappear at 100°C. The weak, resolved bands attributed to the C–N modes indicate that these bonds are in close proximity and likely parallel to the gold surface; however, they are not directly adsorbed to the surface.

An interesting feature lies in the tyrosine residues—a doublet appears at 835 and 855 cm^{-1}. This doublet is sensitive to changes in the local environment, manifested when the ratios of the two bands differ. As can be seen from the activity in the region, denaturation of the protein likely alters the degree to which the tyrosine residues are exposed to aqueous solution and to the gold nanoparticle surface, providing further evidence that the protein is denatured (Lippert et al. 1976; Podstawka et al. 2004; Tu 1982; Yu et al. 1972). Moreover, at 620 and 1,005 cm^{-1}, the phenylalanine ring breathing mode is resolved at room temperature and disappears upon heating to 100°C (Lippert et al. 1976; Podstawka et al. 2004; Tu 1982).

Small bands from 1,500 to 1,580 cm^{-1} in the insulin spectra are resolved at RT. This region represents the amide II band (1,520–1,540 or 1,555–1,560 cm^{-1}) and modes assigned to asymmetric carboxylate stretching vibrations, histidine and/or phenylalanine. Heating the protein to 60°C, the amide II bands disappear, and the shoulder centered at 1,560 and 1,585 cm^{-1}, becomes more resolved and heightens in intensity, implying the carboxylate and histidine and/or phenylalanine are in close proximity to the gold surface (Zhao et al. 2004). In the spectra taken at 100°C, the bands that were enhanced have decreased intensity, with the 1,585 cm^{-1} band disappearing altogether. Furthermore, the proteins likely interact with the gold surface via its carboxyl groups of aspartic and glutamic acid and the C-terminus, as evidenced by the carboxylate stretching, deformation, and wagging vibrations (tentatively assigned to 965, 730 and 620 cm^{-1}, respectively), and/or via the aromatic residues due to the previously mentioned spectral shifts, reflecting different orientation or geometry of the amino acid residues (Miura and Thomas 1995; Miura et al. 2000; Podstawka et al. 2004; Stewart and Fredericks 1999; Tu 1982; Yu et al. 1972).

4 Conclusion

In this paper, an optofluidic device has been described that has proven to improve the detection efficiency, consistency and sensitivity of SERS. The device has been shown to provide characteristic structural information of aqueous samples at ultra-low concentration within minutes. The detection of the protein denaturation is achieved by using the optofluidic device with insulin and BSA as samples. The secondary structural information of protein can be extracted from the SERS data. BSA, composed primarily of α-helices, shows some β-sheet formation with a decrease in α-helical content upon heating. The reduction in the band attributed to phenylalanine supports that the protein has unfolded. However, some secondary structure is still retained since the bands are reduced, but not completely eliminated. On the other hand, insulin demonstrates more pronounced structural changes than BSA, indicating a more intense unfolding of the protein. Activity in the region corresponding to tyrosine, phenylalanine, and carboxylate residues supports denaturation and the protein likely adopting different orientations with respect to the gold surface. Thus, insulin and BSA show conformational changes from α-helix to β-sheet with increased heat as confirmed by monitoring the SERS spectra. The detection volume needed to fill the device was shown to be as low as microliters. With conventional photolithography fabrication processes, the device can be produced at a low cost and for use in high throughput applications. Furthermore, multiple devices can be fabricated on a single wafer. More specifically, 16 or more devices can easily be fabricated on one 4″ wafer, which enables parallel analysis for higher throughput. These advantages show the potential of this optofluidic device for use in bio/chemical detection, especially in diagnostics and prognostics, where the identification of abnormal proteins is needed.

References

Abe H, Manzel K, Schulze W et al (1981) Surface-enhanced Raman spectroscopy of CO adsorbed on colloidal silver particles. J Chem Phys 74:792–797

Campion A, Kambhampati P (1998) Surface-enhanced Raman scattering. Chem Soc Rev 27:241–250

Chaney SB, Shanmukh S, Dluhy RA et al (2005) Aligned silver nanorod arrays produce high sensitivity surface-enhanced Raman spectroscopy substrates. Appl Phys Lett 87(3):031908

Chou I, Benford M, Beier HT et al (2008) Nanofluidic biosensing for β-amyloid detection using surface enhanced Raman spectroscopy. Nano Lett 8:1729–1735

Dick LA, McFarland AD, Haynes CL et al (2002) Metal film over nanosphere (MFON) electrodes for surface-enhanced raman spectroscopy (SERS): improvements in surface nanostructure stability and suppression of irreversible loss. J Phys Chem B 106:853–860

Emory SR, Haskins WE, Nie S (1998) Direct observation of size-dependent optical enhancement in single metal nanoparticles. J Am Chem Soc 120:8009–8010

Félidj N, Aubard J, Lévi G et al (2003) Optimized surface-enhanced Raman scattering on gold nanoparticle arrays. Appl Phys Lett 82:3095–3097

Félidj N, Truong SL, Aubard J et al (2004) Gold particle interaction in regular arrays probed by surface enhanced Raman scattering. J Chem Phys 120:7141–7146

Fleischman M, Hendra PJ, McQuillan AJ (1974) Raman spectra of pyridine adsorbed at a silver electrode. Chem Phys Lett 26:163–166

Gersten J, Nitzan A (1980) Electromagnetic theory of enhanced Raman scattering by molecules adsorbed on rough surfaces. J Chem Phys 73:3023–3037

Gunnarsson L, Bjerneld EJ, Xu H et al (2001) Interparticle coupling effects in nanofabricated substrates for surface-enhanced Raman scattering. Appl Phys 78:802–804

Hering K, Cialla D, Ackermann K et al (2008) SERS: a versatile tool in chemical and biochemical diagnostics. Anal Bioanal Chem 390:113–124

Jiang C, Chang JY (2005) Unfolding and breakdown of insulin in the presence of endogenous thiols. FEBS Lett 579:3927–3931

Kneipp K, Wang Y, Kneipp H (1997) Single molecule detection using surface-enhanced Raman scattering (SERS). Phys Rev Lett 78:1667–1690

Kneipp K, Kneipp H, Kartha VB et al (1998) Detection and identification of a single DNA base molecule using surface-enhanced Raman scattering (SERS). Phys Rev E 57:R6281–R6284

Kneipp K, Kneipp H, Itzkan I et al (1999) Ultrasensitive chemical analysis by Raman spectroscopy. Chem Rev 99:2957–2976

Kneipp K, Kneipp H, Itzkan I et al (2002) Surface-enhanced Raman scattering and biophysics. J Phys Condens Matter 14:R597–R624

Kubo S, Gu Z, Tryk DA et al (2002) Metal-coated colloidal crystal film as surface-enhanced Raman scattering substrate. Langmuir 18:5043–5046

Lippert JL, Tyminski D, Desmueles PJ (1976) Determination of the secondary structure of proteins by laser Raman spectroscopy. J Am Chem Soc 98:7075–7080

Miura T, Thomas GJ (1995) Raman spectroscopy of proteins and their assemblies. Subcell Biochem 24:55–99

Miura T, Suzuki K, Naohio K et al (2000) Metal binding modes of alzheimer's amyloid â-peptide in insoluble aggregates and soluble complexes. Biochemistry 39:7024–7031

Moskovits M (2005) Surface-enhanced Raman spectroscopy: a brief retrospective. J Raman Spectrosc 36:485–496

Nie S, Emory RS (1997) Probing single molecules and single nanoparticles by surface-enhanced Raman scattering. Science 275:1102–1106

Nikoobakht B, El-Sayed EA (2003) Surface-enhanced Raman scattering studies on aggregated gold nanorods. J Phys Chem A 107:3372–3378

Oldenburg SJ, Westcott SL, Averitt RD et al (1999) Surface enhanced Raman scattering in the near infrared using metal nanoshell substrates. J Chem Phys 111:4729–4735

Otto A (2005) The 'chemical' (electronic) contribution to surface-enhanced Raman scattering. J Raman Spectrosc 36:497–509

Pemberton JE, Buck RP (1981) Detection of low concentration of a colored adsorbate at silver by surface-enhanced and resonance-enhanced Raman spectrometry. Anal Chem 53:2263–2267

Pettinger B, Wenneng U, Wetzel H (1980) Surface plasmon enhanced Raman scattering frequency and angular resonance of Raman scattered light from pyridine on Au, Ag and Cu electrodes. Surf Sci 101:409–416

Podstawka E, Ozaki Y, Proniewicz LM (2004) Adsorption of S–S containing proteins on a colloidal silver surface studied by surface-enhanced Raman spectroscopy. Appl Spectrosc 58:1147–1156

Shanmugam G, Polavarapu PL (2004) Vibrational circular dichroism spectra of protein films: thermal denaturation of bovine serum albumin. Biophy Chem 111:73–77

Stevenson CL, Vo-Dinh T (1996) Signal expressions in Raman spectroscopy. In: Lasema JJ (ed) Modern techniques in Raman spectroscopy, 1st edn. Wiley, West Sussex, pp 1–39

Stewart S, Fredericks PM (1999) Surface-enhanced Raman spectroscopy of peptides and proteins adsorbed on an electrochemically prepared silver surface. Spectrochim Acta A 55:1615–1640

Su KH, Wei QH, Zhang X et al (2003) Interparticle coupling effects on plasmon resonances of nanogold particles. Nano Lett 3:1087–1090

Tu AT (1982) Raman spectroscopy in biology. Wiley, New York

Wetzel R, Becker M, Behlke J et al (1980) Temperature behaviour of human serum albumin. Eur J Biochem 104:469–478

Wang H, Levin CS, Halas NJ (2005) Nanosphere arrays with controlled sub-10-nm gaps as surface-enhanced Raman spectroscopy substrates. J Am Chem Soc 127:14992–14993

Wang M, Jing N, Chou I et al (2007) An optofluidic device for surface enhanced Raman spectroscopy. Lab Chip 7:630–632

Yu NT, Liu CS, O'Shea DC (1972) 34-laser Raman spectroscopy and the conformation of insulin and proinsulin. J Mol Biol 70:117–132

Zeman EJ, Schatz GC (1987) An accurate electromagnetic theory study of surface enhancement factors for silver, gold, copper, lithium, sodium, aluminum, gallium, indium, zinc, and cadmium. J Phys Chem 91:634–643

Zhao H, Yuan B, Dou X (2004) The effects of electrostatic interaction between biological molecules and nano-metal colloid on near-infrared surface-enhanced Raman scattering. J Opt A Pure Appl Opt 6:900–905